PolSAR Ship Detection Based on Azimuth Sublook Polarimetric Covariance Matrix

Ziyuan Yang, Lu Fang, Biao Shen, and Tao Liu

***Abstract*—Polarimetric synthetic aperture radar (PolSAR) is an important tool for marine remote sensing. In the past two decades, subaperture decomposition is considered as an alternative method to extract ship targets, especially in complex conditions where the detection based on intensity performs not well. The introduction of polarization information can enhance the detection ability of radar. The combination of sublook techniques and polarization will lead to more precise target extraction. The first methods jointly using information of polarization and sublook is the polarimetric internal Hermitian product (Pol-IHP), which nowadays has been corrected as Pol-HIP. However, it is limited by the number of sublooks and recently developed as generalized multi-sublooks correlation. In this article, a novel sublook polarimetric covariance matrix (SPCM) is established, based on which a sublook-polarimetric whitening filter (sub-PWF) is further proposed for ship detection. The SPCM represents a given pixel using a high-dimensional covariance matrix which utilizes the spectral correlation in imaging progress and the scattering characteristics of different polarization channels. The superiority of sub-PWF based on SPCM is validated via the measured single look complex PolSAR data from RadarSAT-2 and GaoFen-3. Results show this new method can improve the target to clutter ratio and reduce the clutter fluctuation. The ROC curves in both small and large scenes proves that sub-PWF can reach ideal detection performance.**

***Index Terms*—Polarimetric synthetic aperture radar (PolSAR), polarimetric-interferometric, ship detection, subaperture decomposition, sublook polarimetric covariance matrix (SPCM), sublook-polarimetric whitening filter (sub-PWF).**

I. Introduction

POLARIMETRIC synthetic aperture radar (PolSAR) has become a powerful tool of marine remote sensing because of its all-day and all-weather capability and polarization information retaining [1]. The application of PolSAR ship detection is of great importance in both civilian and military fields. Generally, the ship has stronger backscattering signal than the background, therefore the intensity of SAR imagery can be utilized to statistically test whether the pixel is of ship or sea clutter [1]. On the other hand, PolSAR can retain the polarimetric response, which is an important attribute of targets and can be used in ship detection and recognition.

Manuscript received 25 February 2022; revised 2 May 2022 and 18 August 2022; accepted 29 September 2022. Date of publication 3 October 2022; date of current version 11 October 2022. This work was supported in part by the National Natural Science Foundation of China under Grants 62171452 and 61771483. *(Corresponding author: Tao Liu.)*

The authors are with the School of electronic engineering, Naval University of Engineering, Wuhan 430033, China (e-mail: yzy_199702@sina.com; fangluflora@163.com; wyzxdzj@163.com; liutao1018@hotmail.com).

Digital Object Identifier 10.1109/JSTARS.2022.3211431

There is a well-established general consensus that polarimetric information can provide significant benefits in a wide range of applications including ship detection [1], [2], [3], [4], [5], [6], [7], [8], [9]. The optimal polarimetric detector derived from likelihood ratio test and the polarimetric whitening filter (PWF) derived from minimizing fluctuation are two classical methods [3]. Recently, the polarimetric notch filter (PNF) was proposed for ship detection by minimizing sea clutter power [4]. Unfortunately, it also reduces part energy from targets, which has the same physical mechanism as that from clutter. Liu et al. [5] improved the PNF in the multilook case and obtained the novel PNF. Nunziata and M. Migliaccio [6] proposed a dual-polarization model to exploit *X*-band CSK SAR data acquired in the incoherent PingPong to observe targets at sea. The polarimetric cross-entropy is introduced for ship detection because it describes the polarimetric scattering randomness [7]. Migliaccio et al. [8] combines the polarimetric entropy and reflection symmetry for oil slicks and manmade metallic target observation, again showing the importance of polarization. Zhang et al. proposed a polarimetric covariance difference matrix [9] to use the amplitude, phase, and spatial information. On the basis the neighborhood polarimetric covariance matrix is proposed to enhance the matrix property [2]. However, addressing the problems associated with complex sea clutter modeling, slow and small target detection and dense targets separation still remains a challenge in PolSAR ship detection [10]. In the above cases, the confusion of ships and sea clutter leads to a poor performance of constant false alarm rate (CFAR), causing problems such as target merging, splitting and miss alarm [11]. Gui et al. have done in-depth research on the above problems and proposed efficient ship detection using the generalized gamma distribution [12], [13], [14]. For better SAR imagery segmentation, the Kurtosis wavelet energy and Kurtosis curvelet energy are great features to efficiently classify different textures [15], [16]. In addition, there are many ship detection approaches based on the deep learning (DL) nowadays, such as hybrid CNN-MLP classifier [17]. However, to our best knowledge, the open PolSAR benchmark dataset is very few and the DL is data-sensitive.

In the past two decades, subaperture decomposition is considered as an alternative method to extract ship targets, especially in complex conditions where the detection based on intensity performs not well [18], [19], [20], [21], [22]. The first sublook detector is sublook coherence proposed by Arnaud [19]. Two years later Iehara and Ouchi introduced two-dimensional cross correlation function (2-D-CCF) [18], which can work in heavy

sea clutter even the position of ships is slightly shifted in different sublooks. Ouchi et al. conducted further research on this issue, and proved the effectiveness of zero-lag 2-D-CCF [20], [21]. Souyris et al. proposed to replace the sublook coherence by correlation and named this method internal Hermitian product (IHP), which removes the normalization in sublook coherence for utilizing both the amplitude and phase information [22]. Recently, the name "IHP" was pointed out to be inaccurate and should be Hermitian internal product (HIP) by Gierull [23]. Greidanus [24] tried to use three sublooks to jointly detect ship targets and found it performs even worse than multilook processing. Schneider et al. [25] proposed the sublook entropy detector to detect coherent scatterers in urban areas. However, the measured data proved that the sublook entropy is not suitable for ship detection especially when sublooks formed from azimuth direction [26]. Brekke et al. studied the subband extraction strategies and found that partial subaperture overlap provided better ship detection performance [27]. Recently, Sanjuan-Ferrer et al. [28] proposed a new sublook detector based on the generalized likelihood ratio test (GLRT). The GLRT method also seems to perform well in ship detection when the sublooks are formed from range direction [26]. However, the good detection ability of GLRT mainly comes from the CFAR maintenance, rather than the ship detail retention. For subsequent target recognition, in addition to judging whether there is a ship, it is also very important to retain the details of the target. For this issue, Renga et al. [28] introduced the incoherent entropy and designed a segmentation algorithm for maritime traffic monitoring. Gierull [23] provided rigorous theoretical analysis and found that from the existing CFAR model, sublook correlation cannot be demonstrated superior to intensity-based detection. But, it is still necessary to use sublook technology in order to better preserve target details especially when sea conditions are complex, or the intensity-based detection can only confirm a few pixels belong to the ships.

As for the combination of sublook techniques and polarization, Ferro-Famil et al. [30] proposed to use the coefficient of variation (CV) to determine the useful spectrum borders and estimate whitening function along the range direction in range doppler (RD) domain. Then, the H-alpha-A decomposition was operated in each sublooks [30]. In further research, the maximum-likelihood test was applied in nonstationary target detection [31]. However, this approach is more appropriate in farmland. Inspired by the polarimetry-interferometry (POL-IN) [32], Souyris et al. extended their "IHP" method to polarimetric cases and named it "POL-IHP" (corrected to "HIP" by Gierull [23], hereinafter collectively referred to as "pol-correlation"). Pol-Correlation is limited by the sublook number of 2 and its performance in ship detection need to be tested. Schneider et al. used polarimetric entropy and sublook entropy as two independent coordinates to analysis urban area scenes. Wei et al. [33] developed pol-correlation as generalized multisublooks correlation (GMC), which broke through the limitation of two sublooks. Although the sublook number's limitation was broken through, the GMC method is only a generalized coherence of multi sublooks, which does not optimize the polarization state.

Therefore, this article focuses on the features of sublook and polarization. To better combine the sublook techniques and polarization, the main contributions of this article are as follows.

1) The sublook polarimetric covariance matrix (SPCM) is established. The SPCM represents a given pixel using a high-dimensional covariance matrix which utilizes the spectral correlation in imaging progress and the scattering characteristics of different polarization channels.
2) A sublook-PWF (sub-PWF) is further developed based on SPCM. The superiority of sub-PWF based on SPCM is validated via the measured PolSAR data of both small and large scenes.

The remainder of this article is organized as follows. Section II describes the operation of subaperture decomposition, pol-correlation method and GMC method. Section III presents the establishment of SPCM and proposed the sub-PWF. The measured PolSAR data were used to assess different sublook-polarimetric detectors in Section IV and Section V for small and large scenes, respectively. Finally, Section VI concludes the article.

II. Subaperture Decomposition and Sublook-Polarimetric Detectors

As Ouchi et al. mentioned in [20], the sublooks used to detect ships are usually formed in azimuth direction for resolution equality. Meanwhile, the azimuth direction contains more information about target stability in the imaging process and can be used to extract velocity for later research. In the previous studies, it's more about what to do with the generated sublooks, but not much about the decomposition process. Some studies did not remove the carrier frequency of the sublooks, leading to the modulation of the correlation results, some determined the length of the effective signal with the prior information of the sensor and some using fixed window function to handle all data [22], [27], [28], [30]. Therefore, specific operations such as how to determine the useful signal boundary, how to solve the problem of nonzero center frequency of the primitive full aperture and the estimate of window removing function need to be summarized.

A. Subaperture Decomposition

For a given SAR image, it is not easy to obtain the sensor parameters such as the middle frequency, observation angle and windowing functions, especially for space-borne equipment. On the other hand, due to the linearity of standard SAR imaging theory, the sublook images can be generated directly from focused images by calculating FFT along the azimuth direction, removing the windowing and selecting a portion of the full spectrum [26]. The specific steps are shown in Fig. 1. The solid lines represent the flow and dotted lines are connected to the schematic diagram of the corresponding node.

It is obvious that direct spectral segmentation will lead to unstable amplitude of different subbands, so the windowing removal is needed. In standard SAR imaging, the center frequency of azimuth direction signal after down conversion is

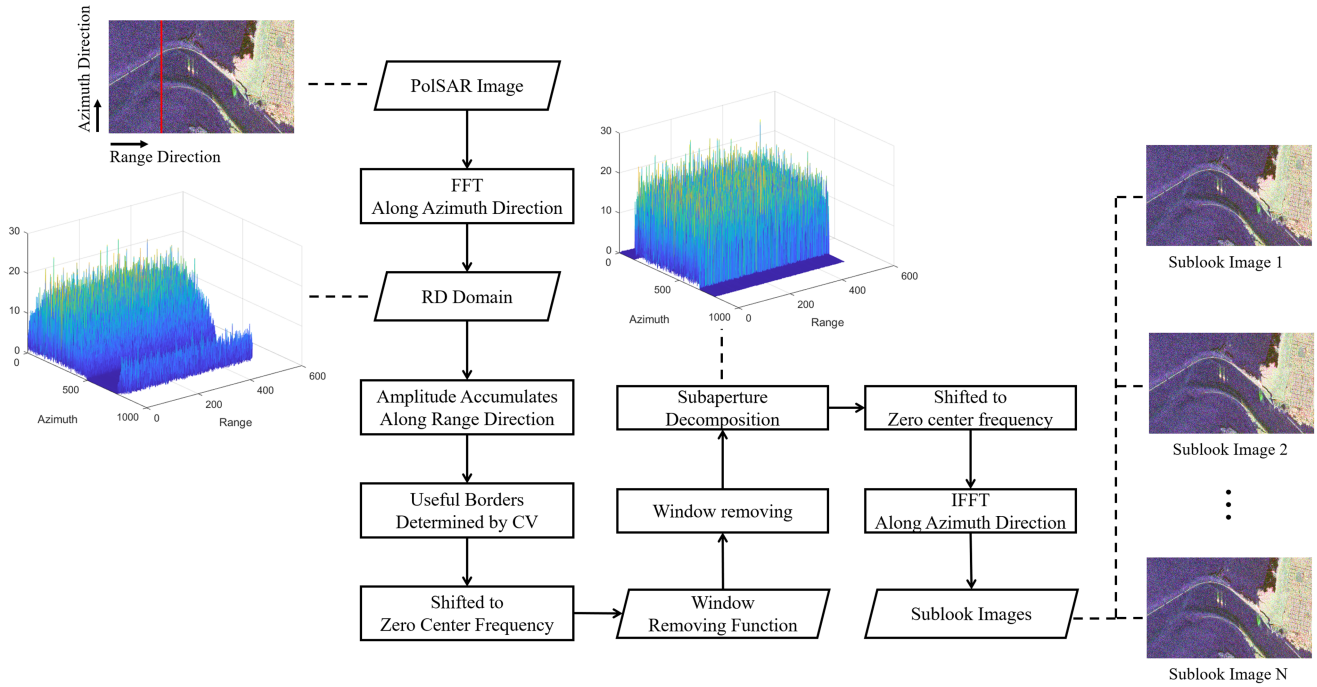

Fig. 1. Flowchart of subaperture decomposition.

zero. However, different sensors have different motion parameters, observation angles and imaging algorithms, therefore the Doppler center of azimuth signal may not be set as zero. With the influence of oversampling, the signal boundary should be determined at first, then the center frequency of the full aperture should be moved to zero before window removal. After azimuth windowing removal, the subbands also need to be shifted to zero center frequency.

No matter in azimuth or in range, the response after pulse compression in the spatial (time) domain can be described as:

$$s(t) = C_0 \sin c\left[B_s\left(t - t_0\right)\right] \exp\left[2\pi f_x\left(t - t_0\right)\right] \tag{1}$$

where C_0 is the complex constant related to the radar system and targets backscattering, B_s is the full bandwidth of azimuth direction and t_0 is the time delay of target, and f_x is the carrier frequency which is difficult to know without prior information.

The RD domain signal are accumulated incoherently along the range direction, and the boundary is determined by the CV on the cumulants:

$$\mathrm{CV} = \frac{\sigma}{\mu} \tag{2}$$

where σ and μ denote the variance and the mean value in the slide-window, respectively.

Then the signal is divided by the normalized cumulants to remove the windowing. Therefore, the stationary RD domain is derived and the subaperture decomposition is operated by subband selection.

After IFFT operation, the generated sublooks have lower resolution, which is related to the bandwidth. The expression of sublooks in spatial (time) domain is

$$s_n(t) = C_n \mathrm{sinc}\left[B_n\left(t - t_0\right)\right] \tag{3}$$

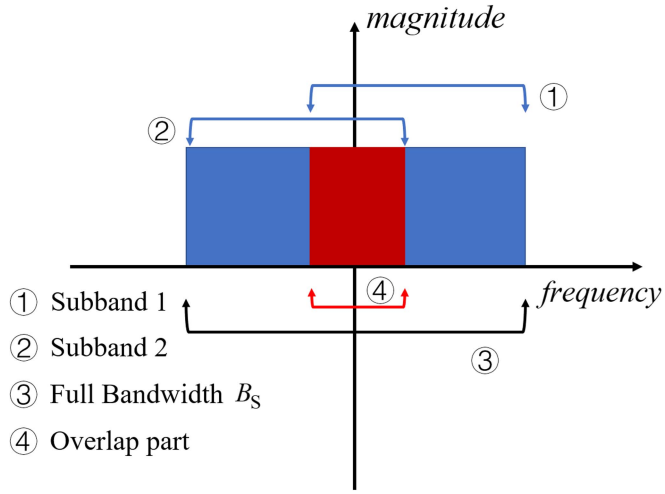

Fig. 2. Schematic diagram of subband overlap.

where the subscript n denotes the nth sublook, C_n is the corresponding complex constant, B_n is the bandwidth of the n-th sublook. The carrier frequency is removed in order to avoid the phase modulation. The relationship between the full bandwidth and subbandwidth is

$$B_n = \frac{B_s}{1 + (N-1)\cdot(1-\gamma)} \tag{4}$$

where N is the number of sublooks and $\gamma(0 < \gamma < 1)$ is the overlap degree, respectively.

Subband overlap is usually adopted for unstable targets [26]. The schematic diagram is as Fig. 2.

B. The Pol-Correlation Method

Pol-correlation is the polarimetric extension of sublook correlation method [22]. It maximizes the Hermitian internal product of 2 sublooks decomposed from PolSAR data, which is essentially a weight optimization problem.

The sublook polarimetric data is expressed as:

$$\mathbf{s}_1 = \left[S_{\mathrm{HH1}}, \sqrt{2}S_{\mathrm{HV1}}, S_{\mathrm{VV1}}\right]^T$$
$$\mathbf{s}_2 = \left[S_{\mathrm{HH2}}, \sqrt{2}S_{\mathrm{HV2}}, S_{\mathrm{VV2}}\right]^T \quad (5)$$

where $\mathbf{s}$ denotes the scattering vector of each sublook. S_{xy} represents the complex element with x standing for the transmitting polarization and y for the receiving polarization. (H horizontal polarization and V vertical polarization). The number in the subscript denotes the corresponding sublook.

The objective of Pol-Correlation is to maximize ρ

$$\rho = \left\langle \mathbf{w}_1^H \mathbf{s}_1 \mathbf{s}_2^H \mathbf{w}_2 \right\rangle = \mathbf{w}_1^H \mathbf{\Omega}_{12} \mathbf{w}_2 \quad (6)$$

where $\mathbf{w}_1$ and $\mathbf{w}_2$ are the normalized weight vector, superscript H denotes the conjugate transpose operation. Symbol $\langle . \rangle$ represents ensemble averaging. $\mathbf{\Omega}_{12} = \langle \mathbf{s}_1 \mathbf{s}_2^H \rangle$ is a 3×3 complex matrix containing the polarization information and interferometric phase relations. $\mathbf{\Omega}_{12}$ is not a standard Hermitian matrix, because $\mathbf{s}_1$ and $\mathbf{s}_2$ are decorrelated outside the particular case of the pure point target [22]. However, the matrices $\mathbf{\Omega}_{12}\mathbf{\Omega}_{12}^H$ and $\mathbf{\Omega}_{12}^H\mathbf{\Omega}_{12}$ are Hermitian.

Suppose the common eigenvalues of $\mathbf{\Omega}_{12}\mathbf{\Omega}_{12}^H$ and $\mathbf{\Omega}_{12}^H\mathbf{\Omega}_{12}$ is v. Souyris et al. [22] derived the relation from Lagrange conditional method that

$$\mathrm{Max}\,(\rho) = \mathrm{Max}\left(\sqrt{v}\right). \quad (7)$$

This method can significantly improve the detection ability in land scenes [22], [33]. However, in sea surface with large Bragg scattering it may not be able to take full advantage of the polarimetric information, which will be proved in later experiments.

C. GMC Method

In order to break the limitation of 2 sublooks, generalized similarity parameter (GSP) is introduced to describe the correlation degree of polarimetric sublooks [33].

The GSP of *N* polarimetric sublooks is defined as

$$|R_g| = \begin{vmatrix} 1 & \frac{\left|\mathbf{s}_1^H \mathbf{s}_2\right|}{\|\mathbf{s}_1\|_2 \|\mathbf{s}_2\|_2} & \cdots & \frac{\left|\mathbf{s}_1^H \mathbf{s}_N\right|}{\|\mathbf{s}_1\|_2 \|\mathbf{s}_N\|_2} \\ \frac{\left|\mathbf{s}_2^H \mathbf{s}_1\right|}{\|\mathbf{s}_2\|_2 \|\mathbf{s}_1\|_2} & 1 & \cdots & \frac{\left|\mathbf{s}_2^H \mathbf{s}_N\right|}{\|\mathbf{s}_2\|_2 \|\mathbf{s}_N\|_2} \\ \vdots & \vdots & \ddots & \vdots \\ \frac{\left|\mathbf{s}_N^H \mathbf{s}_1\right|}{\|\mathbf{s}_N\|_2 \|\mathbf{s}_1\|_2} & \cdots & \cdots & 1 \end{vmatrix} \quad (8)$$

where $\| \cdot \|_2$ denotes the 2 norm of a vector and each element in the matrix is the polarimetric similarity of 2 sublooks. According to the properties of GSP, when the scattering characteristics of all sublooks are the same, all elements of matrix R_g are 1, therefore $|R_g| = 0$; Otherwise, when the scattering characteristics are absolutely different, R_g becomes an identity matrix and $|R_g| = 1$. It can be deduced that the higher the correlation between the sublook, the lower the value $|R_g|$.

Because there exists

$$\begin{aligned} \left|\mathbf{s}_1^H \mathbf{s}_2\right|^2 &= \frac{\left|\mathbf{s}_1^H \mathbf{s}_2\right|^2}{\|\mathbf{s}_1\|_2^2 \|\mathbf{s}_2\|_2^2} \cdot \|\mathbf{s}_1\|_2^2 \|\mathbf{s}_2\|_2^2 \\ &= 1 - \left(1 - \frac{\left|\mathbf{s}_1^H \mathbf{s}_2\right|}{\|\mathbf{s}_1\|_2 \|\mathbf{s}_2\|_2} \cdot \frac{\left|\mathbf{s}_1^H \mathbf{s}_2\right|}{\|\mathbf{s}_1\|_2 \|\mathbf{s}_2\|_2}\right) \\ &= \left(1 - \begin{vmatrix} 1 & \frac{\left|\mathbf{s}_1^H \mathbf{s}_2\right|}{\|\mathbf{s}_1\|_2 \|\mathbf{s}_2\|_2} \\ \frac{\left|\mathbf{s}_2^H \mathbf{s}_1\right|}{\|\mathbf{s}_2\|_2 \|\mathbf{s}_1\|_2} & 1 \end{vmatrix}\right) \cdot \|\mathbf{s}_1\|_2^2 \|\mathbf{s}_2\|_2^2 . \\ &= (1 - |R_g|) \cdot \|\mathbf{s}_1\|_2^2 \|\mathbf{s}_2\|_2^2 \end{aligned} \quad (9)$$

Equation (9) is extended to multisublooks situation and the GMC is defined as

$$G = \log\left(\prod_{i=1}^{N} \|\mathbf{s}_i\|_2^2 \cdot (1 - |R_g|)\right) \quad (10)$$

where the $\prod_{i=1}^{N} \|\mathbf{s}_i\|_2^2$ contains the intensity information and $1 - |R_g|$ denotes the correlation degree of multisublooks. In [33], the detectors adopted log scale. For the same measurement with other detectors, (10) is further modified as

$$G = \prod_{i=1}^{N} \|\mathbf{s}_i\|_2 \cdot (1 - |R_g|). \quad (11)$$

Compared with the pol-correlation, GMC doesn't optimize the weights of scattering vector, but it can give the overall correlation of multisublooks of PolSAR data.

III. Sublook Polarimetric Covariance Matrix and Sublook Polarimetric Whitening Filter

A. Establishment of SPCM

Traditionally a PolSAR image pixel is characterized by the scattering vector $\mathbf{s}$, and a pixel patch is characterized by a polarimetric covariance matrix $\mathbf{C}$. Although $\mathbf{C}$ can depict the second-order polarimetric statistics [2], it cannot jointly express the sublook correlation and polarization information.

It is expected that for a set of multisublooks, a combined vector $\mathbf{p}$ can express the pixel

$$\mathbf{p}^T = \left[\mathbf{s}_1^T, \mathbf{s}_2^T, \ldots, \mathbf{s}_N^T\right]. \quad (12)$$

The vector $\mathbf{p}$ is assumed to be a complex circular Gaussian distribution because it is composed of the vector $\mathbf{s}$.

The establishment of SPCM is shown in Fig. 3, the SPCM can be calculated as follows:

$$\mathbf{C}_{sp} = \frac{1}{L} \sum_{i=1}^{L} \mathbf{p}_i \mathbf{p}_i^H \quad (13)$$

where L is the number of looks. The dimension of the SPCM $\mathbf{C}_{sp}$ is $3N \times 3N$.

The probability density function of the SPCM is the complex Wishart distribution, which is a classical model in PolSAR

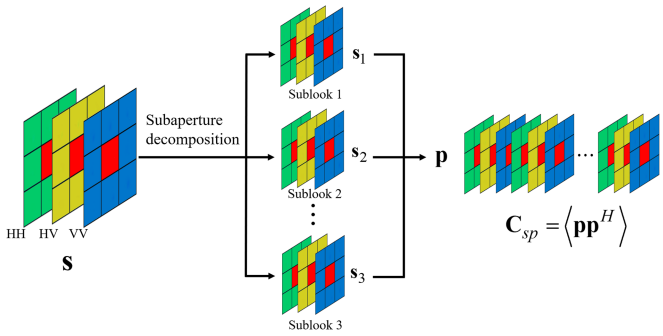

Fig. 3. Flowchart of subaperture decomposition to generate sublook images.

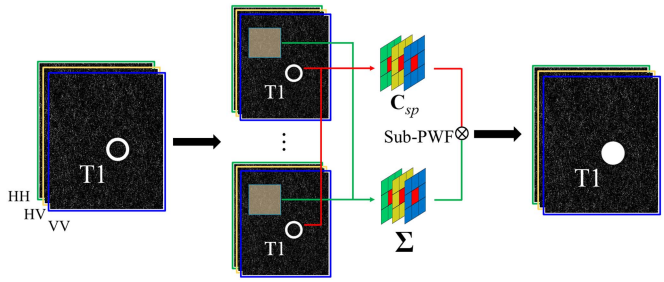

Fig. 4. Flowchart of sub-PWF detector.

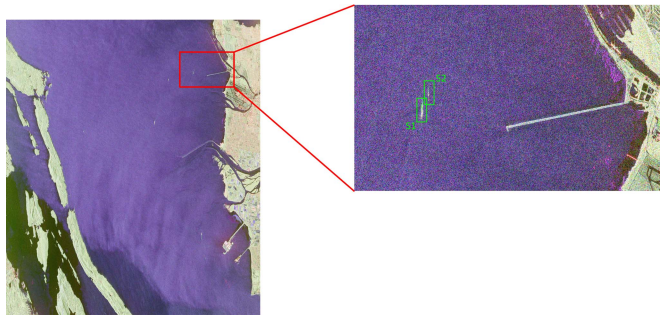

Fig. 5. Pauli-RGB imagery of the Strait of Georgia acquired by RS-2.

family:

$$f(\mathbf{C}_{sp}) = \frac{L^{Ld}|\mathbf{C}_{sp}|^{L-d}\exp\left(-L\cdot\mathrm{tr}\left(\mathbf{\Sigma}^{-1}\mathbf{C}_{sp}\right)\right)}{\Gamma_d(L)|\mathbf{\Sigma}|^{L}} \tag{14}$$

where L is the number of looks, d is the dimension of $\mathbf{C}_{sp}$, and $\mathrm{tr}(\cdot)$ is the trace operator, and $\Gamma_d(L)$ is

$$\Gamma_d(L) = \pi^{\frac{1}{2}d(d-1)}\Gamma(L)\cdots\Gamma(L-d+1). \tag{15}$$

$\Gamma(\cdot)$ is the gamma function. $\mathbf{\Sigma} = \mathrm{E}\{\mathbf{C}_{sp}\}$ is the statistical mean of the SPCM. If the texture is not constant in practice, the multivariate product model can be used to depict more complicated statistics of the sea clutter [34].

B. Sub-PWF Based on SPCM

A pixel is represented by a high dimensional vector $\mathbf{p}$ and the SPCM $\mathbf{C}_{sp}$ depict the second-order statistics. Assume $\mathbf{F}$ is the space transformation matrix, the quadratic form can be defined as

$$\begin{aligned} z &= \frac{1}{L}\sum_{i=1}^{L}(\mathbf{F}\mathbf{p}_i)^H\cdot(\mathbf{F}\mathbf{p}_i) \\ &= \frac{1}{L}\sum_{i=1}^{L}\mathbf{p}_i^H\mathbf{F}^H\cdot\mathbf{F}\mathbf{p} \\ &= \mathrm{tr}\left(\mathbf{M}\mathbf{C}_{sp}\right). \end{aligned} \tag{16}$$

Inspired by the PWF [3], the fluctuation of clutter (i.e., the CV of z) reaches the minimum when $\mathbf{M} = \mathbf{\Sigma}^{-1}$, and the output z obeys a Gamma distribution in homogeneous sea clutter

$$z \sim \gamma\left(Ld, \frac{1}{L}\right) \tag{17}$$

where $\gamma(\alpha,\beta)$ denotes Gamma distribution of which the shape parameter is α, and scale parameter is β.

Fig. 4 displays the flowchart of sub-PWF detector. The polarimetric sublooks pixels are chained together to generate high dimensional vector $\mathbf{p}$ after subaperture decomposition introduced in Section II-A, then the estimation of $\mathbf{\Sigma}$ is conducted from a clutter region and Sub-PWF is operated pixel by pixel. Finally, the output is calculated as (16) and can be used for ship detection.

IV. Validation by Measured Data in Small Scenes

A. Measured Data Descriptions

The first small scene of real PolSAR data is from the Strait of Georgia near Vancouver acquired by RadarSAT-2 (RS-2) in C-band (radar center frequency $5.4\,\mathrm{GHz}$), which has been utilized as a ship detection study site for many years [35], [36]. It has been proven that the mix of vessels and availability of truth data make this an ideal location for detailed analysis of ship detection [37]. The RS-2 FQ18WS data with $9\,\mathrm{m}\times 9\,\mathrm{m}$ resolution and 39° incidence angle is used in small scenes experiments. Its acquisition took place in windy conditions (wind speed ranging from 10 to 13 m/s) on December 19, 2010. The Canadian coast guard monitoring data and AIS information jointly ensured the ship information on PolSAR image [36].

As shown in Fig. 5, there are two ships in the small scene for accurate test. *S*1 is a Tug named "Island Monarch" with 4 m/s speed and *S*2 is a small warship without AIS.

The second small scene is the South China Sea from GaoFen-3 (GF-3) on January 1, 2017, which also works in *C*-band [11]. The scene ID is 3180124 and the incidence angle is 42°. The retrieved wind speed is about 11 m/s [38], and the ground truth is obtained by the same way addressed in the RS-2 dataset [11].

Fig. 6 presents the GF-3 image. The blue rectangle identifies the biggest oil platforms, the red rectangle identifies three ships for detailed analysis.

B. Performance Indexes

The following factors are used to assess the detector performance over the small scenes for detailed analysis.

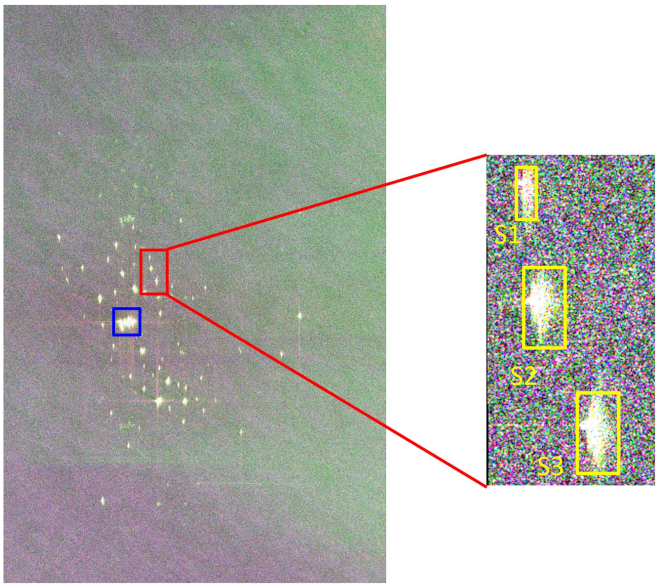

Fig. 6. Pauli-RGB imagery of the oil platforms acquired by GF-3.

1) ROC curves based on pixels to reflect the detection performance and details retaining ability [38].
2) Target to clutter ratio (TCR) to show the contrast between ships and sea clutter

$$\mathrm{TCR} = \frac{\mu_t}{\mu_c} \tag{18}$$

where μ_t and μ_c are the mean value of target and clutter region, respectively.
3) CV, which is a traditional measure of heterogeneity

$$\mathrm{CV} = \frac{\sigma_c}{\mu_c} \tag{19}$$

where the σ_c is the variance of clutter region. The area size for regions study of index (2) (3) is 128×128 pixels in RS-2 dataset and 64×64 in GF-3 dataset.

C. Experiments in RS-2 Dataset

1) Performance Analysis of Pol-Correlation: The single look complex data are decomposed to several subapertures to form sublooks in each polarization channels, and different sublook-polarimetric detectors are used to extract ships in the scene. For convenience, the subband overlap is 0, which will be studied in later separate part. All the number of looks is 5×5.

Fig. 7 presents the ROC curves of pol-correlation versus single polarization sublook correlation. "Pd" is the probability of detection (PD), "Pfa" is the probability of false alarm (PFA). "HH," "HV," "VV" denotes the magnitude detection of different polarization channel. The "Sub-Corr" denotes sublook correlation, "Pol-Col" denotes Polarimetric-Correlation, "Span" is the power synthesized image. From the ROC curves, it is obvious that the sublook correlation improves the detection ability compared to magnitude detection in each polarization channels. HV-sublook correlation gives the best performance compared to other channels. The fact pol-correlation detector

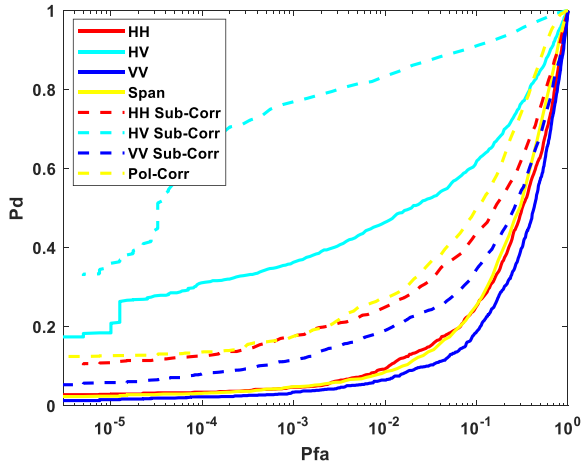

Fig. 7. ROC curves of sublook correlation detectors in the RS-2 image.

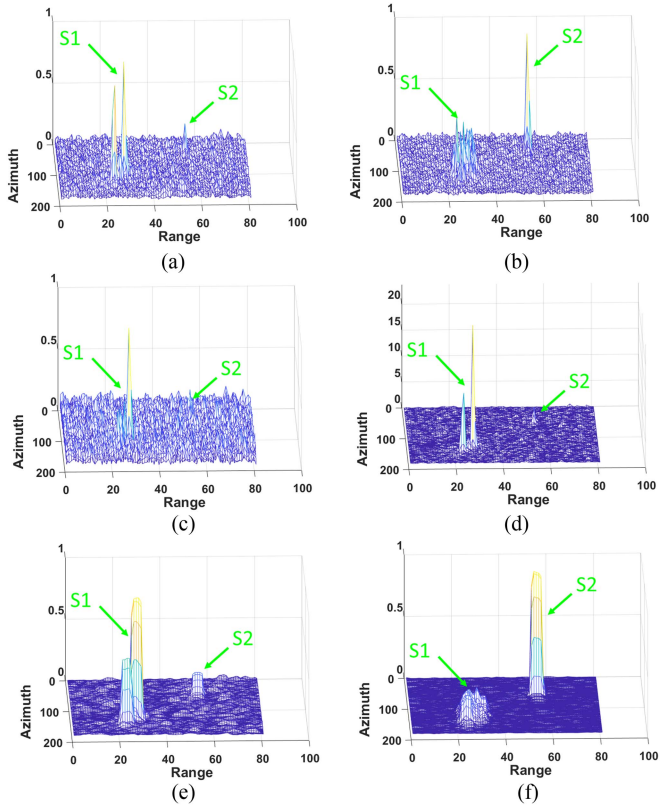

Fig. 8. Normalized detection maps of the RS-2 small scene. (a) HH Channel. (b) HV Channel. (c) VV Channel. (d) Span. (e) Pol-Correlation. (f) HV Sub-Corr.

ranks third in Fig. 7 shows that this method fails to take full advantage of the polarimetric information in ship detection, which performs even worse than detections conducted on HV magnitude.

To better analyze the results, Fig. 8 shows the normalized detection maps and Table I gives the TCR and CV of the tug *S*1 and small ship *S*2.

Due to the Bragg scattering on the surface, HV channel performs better than HH and VV, and HV sublook correlation

TABLE I
TCR AND CV OF CORRELATION DETECTION RESULTS

	TCR1 (dB)	CV1	TCR2 (dB)	CV2
HH	1.8682	0.5384	0.7970	0.5347
HV	5.0632	0.5495	3.3679	0.5551
VV	0.9721	0.5271	0.5158	0.5379
Span	4.9365	0.9603	2.1252	0.9789
HH Sub-Corr	9.1893	0.6390	2.6833	0.6438
HV Sub-Corr	10.7096	0.7801	13.1915	0.8334
VV Sub-Corr	5.5777	0.6223	1.4859	0.5658
Pol-Corr	7.2286	0.5340	3.7923	0.5036

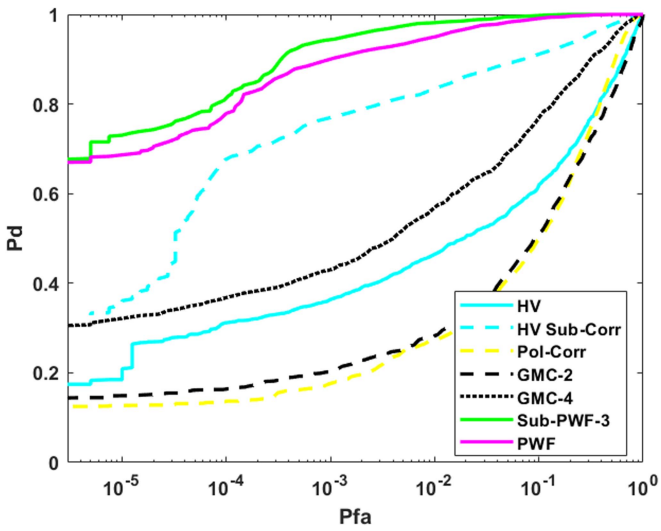

Fig. 9. ROC curves of different sublook polarimetric detectors (RS-2).

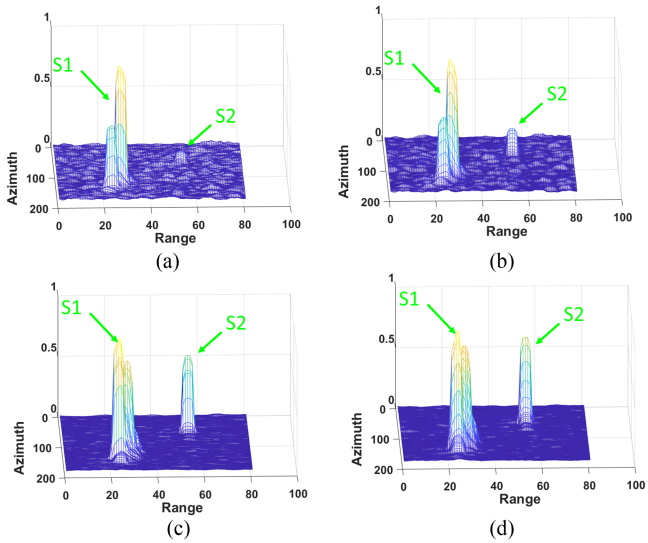

Fig. 10. Normalized detection maps for sublook-polarimetric detectors. (a) GMC-2. (b) GMC-4. (c) PWF. (d) Sub-PWF-3.

TABLE II
TCR AND CV OF SUBLOOK-POLARIMETRIC DETECTION RESULTS

	TCR1 (dB)	CV1	TCR2 (dB)	CV2
GMC-2	4.7507	0.3036	1.4956	0.2559
GMC-4	5.5087	0.2442	2.7810	0.2163
PWF	9.7691	0.2683	7.5409	0.2297
Sub-PWF-3	9.3310	0.2721	7.3630	0.2014

is even better than pol-correlation, which indicates that pol-correlation increases the polarimetric interference of sea clutter while increasing that of targets, causing a performance deterioration. The single polarization sublook correlation magnify both the TCR and CV, while pol-correlation maintain the clutter fluctuation. Comparing pol-correlation with HV magnitude, the pol-correlation has higher TCR and similar CV, but it is not as good as HV in ROC curves. It can be found that although a few ship pixels have strong intensity, the refined detection cannot rely on only these pixels. As Novak noted in [3], target detection doesn't absolutely depend on TCR and CV and there exists other factors, such as clutter parameter estimation, scattering characteristics and dataset etc. The pol-correlation can effectively magnify specific structures of ships in PolSAR images, but it is not enough to retain details.

2) Comparisons of Different Sublook-Polarimetric Detectors: Different sublook polarimetric detectors are compared. In order to investigate the influence of polarimetric and sublook information, the PWF is used as the comparison item.

The ROC curves are plotted in Fig. 9. The GMC-X means GMC methods based on *X* sublooks, so does sub-PWF. It can be seen that the sub-PWF performs best, followed by PWF and HV sublook correlation. The GMC do improve the ship detection ability compared to pol-correlation [33], but it still fails to break the limitation of polarimetric advantage of HV channel. The fact that PWF is superior than HV sublook correlation shows that the detection gain caused by polarization is larger than sublooks. Among all the techniques combing polarization and sublook correlation, the sub-PWF based on SPCM improves detection ability on both sides.

The normalized detection maps of GMC, PWF and sub-PWF are shown in Fig. 10. Table II gives the TCR and CV of the detection maps from GMC, PWF, And sub-PWF.

The results show that GMC-2, GMC-4, PWF, and sub-PWF-3 have lower clutter fluctuation than pol-correlation and lower TCR than HV sublook correlation. The TCR of PWF and sub-PWF is close and their detection abilities reflected by ROC curves are better than other detectors. It is also known the TCR and CV are not the only factors that affect the ship detection performance due to the influence of parameter estimation, scattering characteristics and dataset, etc. This leads to the phenomenon that the PWF has the better TCR and even lower CV but it can't reach the better detection performance compared with the Sub-PWF. Some pixels of ships in PWF detection map may have strong intensity and improve the averaged TCR value, but the refined detection cannot rely on only these strong pixels.

Compare all the sublook polarimetric detectors, it is found that the pol-correlation method also improves the coherence of sea clutter while maximizing the coherence of ships with the maximum polarimetric interferometry as its objective function. In the detection of ships on the surface, the pol-correlation often performs worse than the single polarization sublook detectors in HV channel. Meanwhile the pol-correlation cannot break the limitation of the sublook number of 2. GMC can use more

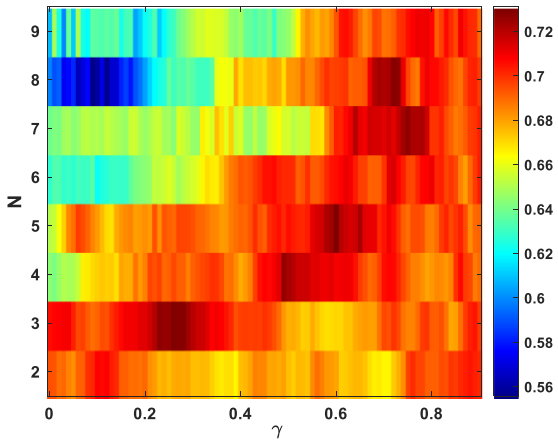

Fig. 11. Detection ability with different N and γ (RS-2).

TABLE III
TOP TEN PD WITH THEIR CORRESPONDING N AND γ (RS-2)

PD	N	γ	Subbandwidth
0.7311	5	0.60	$B/2.60$
0.7303	3	0.26	$B/2.48$
0.7295	3	0.27	$B/2.46$
0.7295	3	0.28	$B/2.44$
0.7295	8	0.72	$B/2.96$
0.7287	3	0.23	$B/2.54$
0.7279	8	0.73	$B/2.89$
0.7279	7	0.75	$B/2.50$
0.7272	3	0.25	$B/2.50$
0.7272	4	0.49	$B/2.53$

than two sublooks to detect ships, but cannot optimize the polarimetric state. The SPCM containing information about both the sublook and polarization and jointly breaking through the number limitation and optimizing the polarimetric state, which is the theoretical basis of its better performance.

3) Analysis of the Sublook Number and Overlap Degree: All the sublook techniques are affected by the sublook number and overlap degree. Gierull [23] noted that an excessive sublook number is detrimental to target detection because of the decrease of TCR. In order to further investigate the impact of sublook number N and overlap degree γ to the sub-PWF based on SPCM, the PFA is fixed as 10^{-5} here to test different PD with their corresponding N and γ. In this experiment, N goes from 2 to 9 and γ goes from 0 to 0.9 at 0.01 intervals. The search results are shown in Fig. 11. Table III lists the top ten PD with their corresponding N and γ, as well as the sub-bandwidth calculated according to (4).

From Fig. 11 and Table III, it can be concluded that due to the spectral instability of small targets, the sublook number more than 2 can indeed improve the detection ability.

Each N and γ can determine a sub-bandwidth. The relationship between sub-bandwidth and detection performance in Fig. 11 is drawn as a scatter diagram, as shown in Fig. 12.

From both Figs. 11 and 12 it can be found that there exists a positive correlation between overlap degree and detection

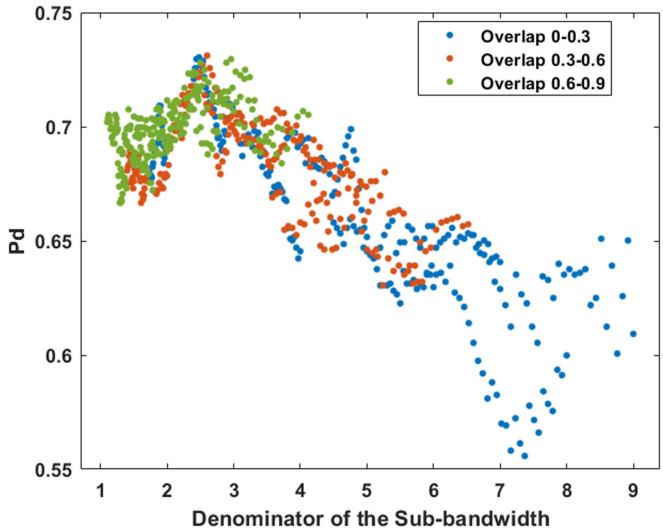

Fig. 12. Relationship of PD and subbandwidth (RS-2).

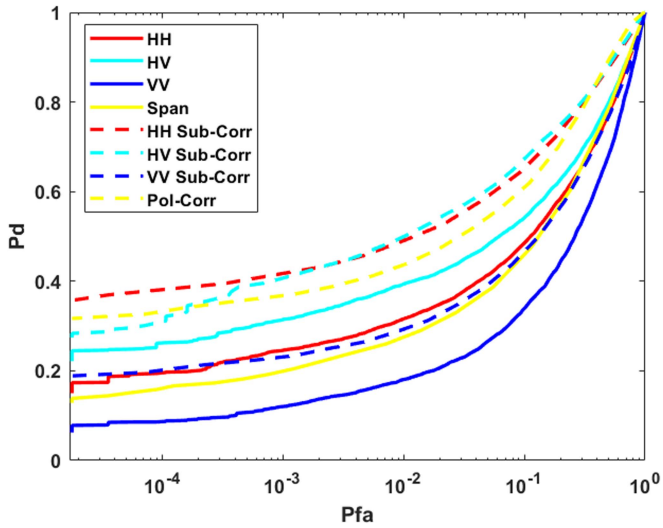

Fig. 13. ROC curves of sublook correlation detectors in the GF-3 image.

ability, but with the increase of N the subbandwith gradually decrease and therefore the detection ability deteriorates. From the density of scatter distribution and the corresponding detection ability, it can be further discovered that the sub-bandwidth, which is directly related to the radar incident angle, target size and the resolution of sublook images, is more determinant to the final results.

D. Experiments in GF-3 Dataset

In order to test the above theory in small scenes of different platforms, the GF-3 imagery is used to repeat the experiments on the RS-2 imagery.

1) Performance Analysis of Pol-Correlation: The ROC curves of Pol-Correlation Vs. single polarization sublook correlation method based on GF-3 dataset are shown in Fig. 13.

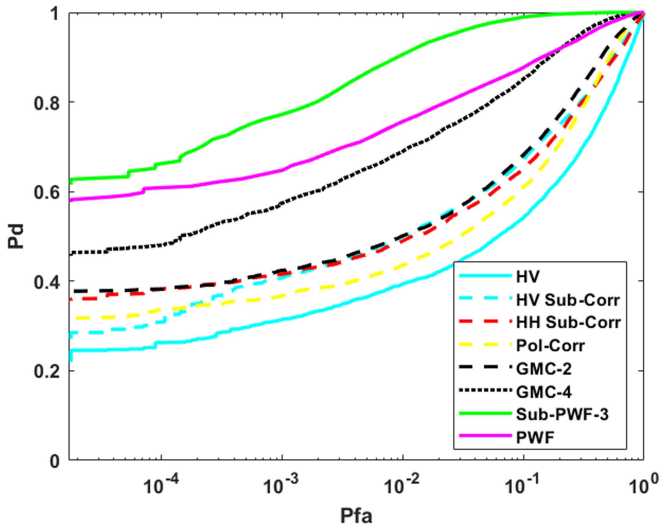

Fig. 14. ROC curves of different sublook polarimetric detectors (GF-3).

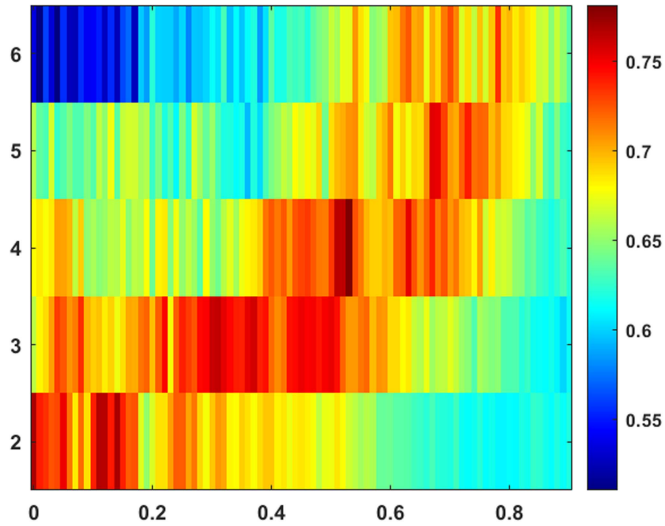

Fig. 15. Detection ability with different N and γ (RS-2).

The sublook overlap degree is 0, the same as correlation analysis of RS-2. It can be seen that Pol-Correlation still performs worse than single channel sublook correlation methods, which is consistent with that in RS-2 dataset. The starting point of the abscissa is not consistent with the RS-2 experiment because the pixel numbers in different scenes are different.

With the increase of PFA, sublook correlation of HV and HH channel has little difference, but both of them are stronger than Pol-Correlation. This fact fully proves that the pol-correlation cannot take full advantage of polarization in the detection of ships on the sea surface.

The detection maps are similar to those in RS-2, which is not shown here for simplicity.

2) Comparisons of Different Sublook-Polarimetric Detectors: Different sublook polarimetric detectors are compared using GF-3 dataset. The overlap degree of sub-PWF is 0 and its sublook number is 3. Further analysis about N and γ would be made later. The ROC curves are shown in Fig. 14 .

It can be seen that sub-PWF performs the best, followed by PWF and GMC-4. The gain of detection ability mainly comes from the combination of polarimetric and sublook information contained by SPCM. Different from RS-2 experiment, the GMC-4 is better than the sublook correlation, which is relevant to radar incident angle, platform attitude and ship material.

3) Analysis of the Sublook Number and Overlap Degree: In order to test the influence of sublook number N and overlap degree γ. The PFA is fixed as 10^{-4} here because the size of GF-3 imagery is smaller than RS-2. N goes from 2 to 6 and γ goes from 0 to 0.9 at 0.01 intervals. The search results are shown in Fig. 15. It follows a similar trend to Fig. 11, with PD values increasing to the upper right with N and γ. Table IV gives the top ten PD with their corresponding N and γ, as well as the sub-bandwidth calculated according to (4). To better investigate the influence factor, the relationship between sub-bandwidth and detection performance are shown in Fig. 16.

TABLE IV
TOP TEN PD WITH THEIR CORRESPONDING N AND γ (GF-3)

PD	N	γ	Sub-bandwidth
0.7810	4	0.53	$B/2.41$
0.7686	2	0.14	$B/1.86$
0.7683	2	0.00	$B/2.00$
0.7667	2	0.11	$B/1.89$
0.7651	2	0.12	$B/1.88$
0.7648	4	0.51	$B/2.47$
0.7631	4	0.52	$B/2.44$
0.7623	3	0.31	$B/2.38$
0.7618	3	0.30	$B/2.40$
0.7581	3	0.37	$B/2.26$

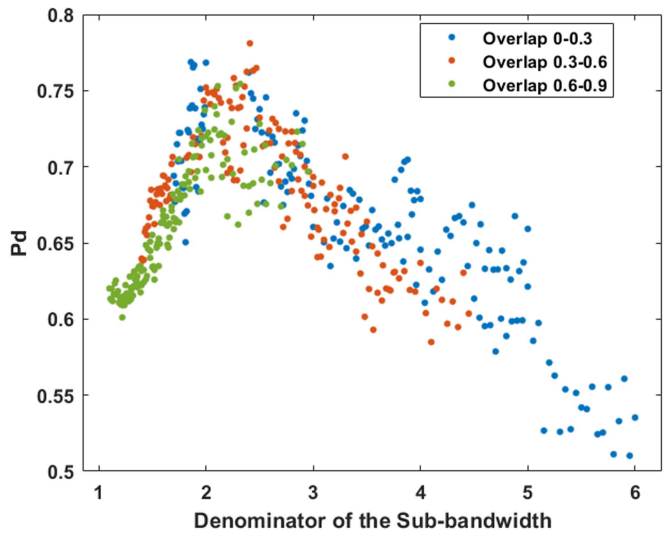

Fig. 16. Relationship of PD and subbandwidth (GF-3).

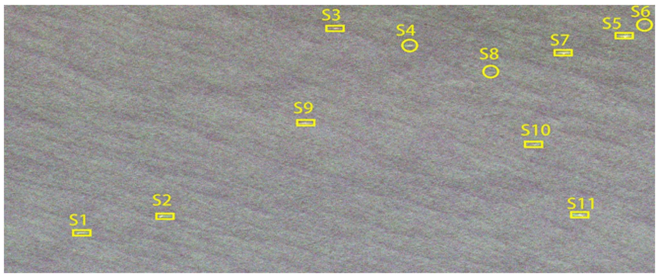

Fig. 17. Pauli-RGB imagery of the selected RS-2 dataset.

From the above results, it can be concluded that N, γ and sub-bandwidth all have impact on detection ability. Although there are many variations in sublook number and overlap degree, the variation of sub-bandwidth is within a certain range. In addition, in the case of fixed bandwidth, the detection ability is different with different N and γ , which is caused by spectrum instability.

V. Validation by Measured Data in Large Scene

In addition to the detailed inspections in small scenes, the capabilities of the sublook-polarimetric detectors in the wide-area scenes also need to be examined. Two large scenes are used in this part.

The first large scene is derived from the Canada North Sea from RS-2 observations during 2013/11. The incidence angle is approximately 32°, covering a square of 25 × 25 km, with a slant range resolution of 5.2 m and azimuth resolution of 7.6 m [38], [40]. The retrieved wind speed is approximately 16 m/s, showing the sea state to be moderate to high [38], [40]. AIS positions of the vessels are acquired and used for the validation [2]. The scene presents 11 ships as shown in Fig. 17.

The measured data is processed using different polarimetric detectors. It is known to all that ship detectors in wide-area surface will inevitably produce blurring. When the several pixels are close, the detection results of these separated pixels can merge into a single blob. To avoid this, we adopted a density-based algorithm to discover erring clusters in large spatial databases with noise (DBSCAN [40]). DBSCAN has two parameters, MinPts, and ε: MinPts, the minimum number of points in a circle with a radius of ε. Additionally, DBSCAN shows an easier way to ships and false alarms [2]. For more accurate clustering, here the distance parameter ε is 100 and the point number is 10 in DBSCAN algorithm [40].

To access the detector performance for measured data, two factors are used to describe the results: the ROC curves and the figure of merit (FOM).

The FOM is an macroscopical index for performance evaluation based on the target number of the final detection map [9]

$$\text{FoM} = \frac{N_{td}}{(N_{fa} + N_{gt})} \tag{20}$$

where N_{td} is the number of detected targets, N_{fa} is the number of false alarms, and N_{gt} is the total number of targets in this scene. Binary search method is used to find appropriate threshold to maintain the N_{fa} as 1.

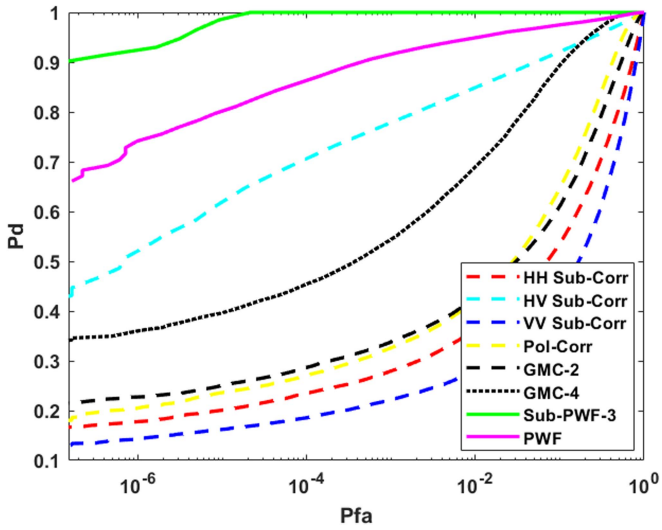

Fig. 18. ROC curves of the RS-2 large scene.

TABLE V
FOM of Detectors for the RS-2 Large Scene

Detector	N_{td}	N_{fa}	$FoM(\%)$
HH Sub-Corr	10	1	76.92%
HV Sub-Corr	12	1	92.31%
VV Sub-Corr	9	1	69.23%
Pol-Corr	10	1	76.92%
GMC-2	10	1	76.92%
GMC-4	10	1	76.92%
Sub-PWF-3	12	1	92.31%
PWF	12	1	92.31%

Fig. 18 shows the ROC curves of different detectors using sublook techniques. It can be seen that the sub-PWF performs the best, followed by PWF, HV sublook correlation and GMC-4. The results of the large scene ROC curves are consistent with the RS-2 small scene results. Pol-correlation does not show very good ship detection ability. Due to the combination of sublook and polarimetric information, sub-PWF achieves the best performance in sublook detectors.

In order to observe the detection results of large scenes from a macroscopic perspective, Fig. 19 shows the detection results of different sublook detectors clustered by the DBSCAN method ("−1" is for false alarms, and other numbers are the detected ships after clustering). For brevity, only figures for sub-PWF and PWF are shown.

There have 12 targets in this article. It should be noted that only 11 ships had AIS certification [40]. Because each effective detector found the twelfth ship, we assume it is the 12th ship.

Binary search method is used to find appropriate threshold to maintain the N_{fa} as 1. Table V gives the FOM of different sublook detectors in RS-2 large scene.

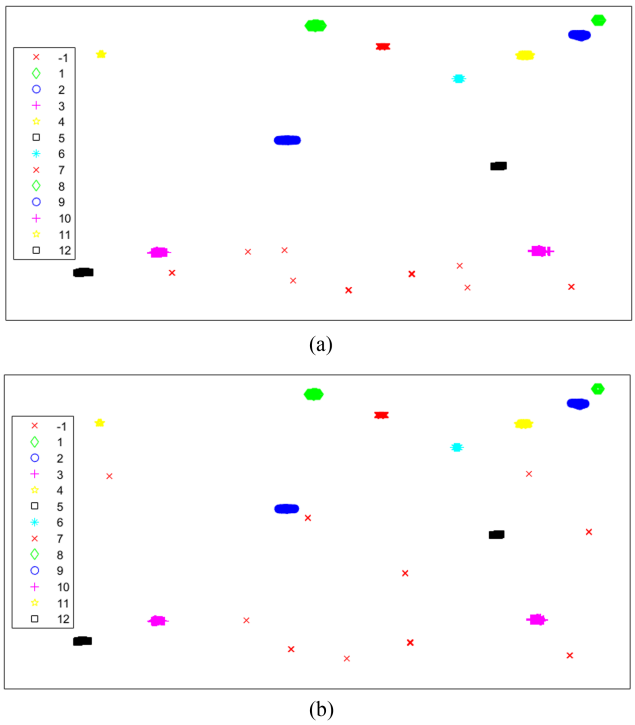

Fig. 19. Results of different detectors in the RS-2 image ("-1" is for false alarms and others "1–12" are the detected ships after clustering). (a) Sub-PWF. (b) PWF.

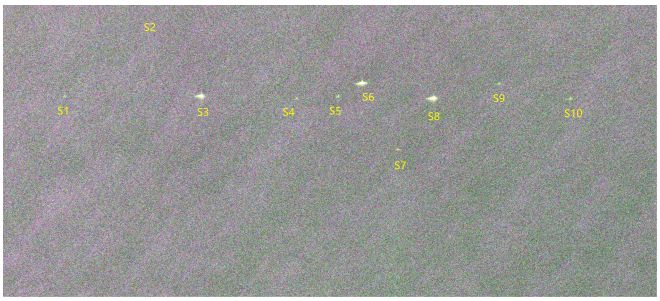

Fig. 20. Pauli-RGB imagery of the selected GF-3 dataset.

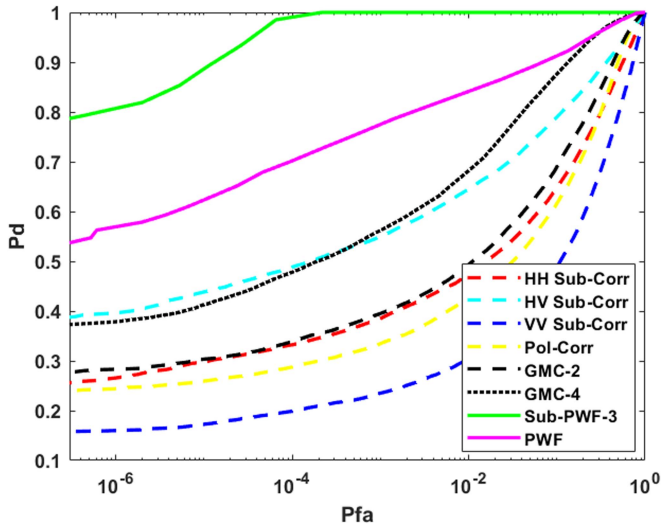

Fig. 21. ROC curves of the GF-3 large scene.

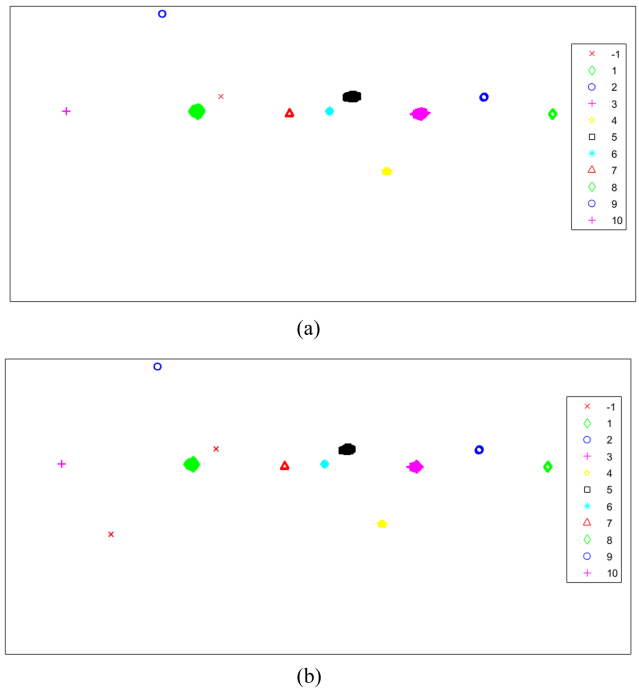

Fig. 22. Results of different detectors in the GF-3 image ("−1" is for false alarms and others "1–10" are the detected ships after clustering). (a) Sub-PWF. (b) PWF.

It can be seen that the Sub-PWF, PWF and HV sublook correlation method give the best FOM 92.31%, pol-correlation, HH sublook correlation, GMC-2 and GMC-4 give the second FOM 76.92%, and VV sublook correlation gives the worst FOM 69.23%. The ranking trend of FOM and ROC curves is the same. The slight difference may lie in the fact that each ship's FOM involving many pixels could be counted as one target.

As shown in Fig. 20, the second large scene contains ten man-made objects with 17 m/s retrieved wind in the South China Sea captured by GF-3 [11], which was taken at the same mission as Fig. 6, that is, they were extracted from the same ultra-wide image. The rectangular boxes represent large targets and circles represent small targets that are difficult to detect.

Fig. 21 shows the ROC curves of different detectors. It can be seen that the sub-PWF performs the best, followed by PWF. Different from RS-2 large scene, GMC-2 and HV sublook correlation have similar ROC curves.

Fig. 22 shows the detection results of different sublook detectors clustered by the DBSCAN method. For brevity, only figures for sub-PWF and PWF are shown.

Table VI gives the FOM of different sublook detectors.

Sub-PWF and PWF give the best FOM 90.91%, followed by HV sublook correlation's 81.82%. The FOM is an macroscopical index for performance evaluation based on the target number of final detection map while ROC curves based on pixels.

TABLE VI
FOM OF DETECTORS FOR THE GF-3 LARGE SCENE

Detector	N_{td}	N_{fa}	$FoM(\%)$
HH Sub-Corr	5	1	45.45%
HV Sub-Corr	9	1	81.82%
VV Sub-Corr	4	1	36.36%
Pol-Corr	6	1	54.55%
GMC-2	5	1	45.45%
GMC-4	4	1	36.36%
Sub-PWF-3	10	1	90.91%
PWF	10	1	90.91%

The results show that sub-PWF is suitable for both fine detection and macroscopical wide area detection. Therefore, it can be concluded that in both small and large scenes, the sub-PWF based on SPCM can effectively detect ships while effectively preserved target details.

VI. CONCLUSION

This article focused on PolSAR ship detection based on sublook techniques. First of all, the subaperture decomposition techniques of PolSAR image is summarized. Second the Pol-Correlation and GMC method is analyzed. Then, the sub-PWF based on SPCM combing the sublook techniques and polarization is proposed. The results show that the detection gain caused by polarization is larger than that of sublooks. Additionally, it is found that the pol-correlation method also improves the coherence of sea clutter while maximizing the coherence of ships with the maximum polarimetric interferometry as its objective function. In the detection of ships on the surface, the pol-correlation often performs worse than the single polarization sublook detectors in HV polarimetric channel.

The SPCM represents a given pixel using a high-dimensional covariance matrix which utilizes the spectral correlation in imaging progress and the scattering characteristics described by different polarization channels. The superiority of sub-PWF based on SPCM is validated via the measured PolSAR data of both small and large scenes. Generally speaking, the sub-PWF based on SPCM can effectively detect ships while effectively preserved target details.

In our future work, we will aim to step into statistical modeling of all these sublook-polarimetric detectors and hope to introduce prior information to design new detectors, which will be integrated into the big family of PolSAR statistical theory. On the other hand, ship detection, velocity estimation and ocean current inversion of multichannel polarimetric along-track interferometric SAR are also the focus of our research.

REFERENCES

[1] T. Liu, Z. Yang, J. Yang, and G. Gao, "CFAR ship detection methods using compact polarimetric SAR in a K-wishart distribution," *IEEE J. Sel. Topics Appl. Earth Observ. Remote Sens.*, vol. 12, no. 10, pp. 3737–3745, Oct. 2019, doi: 10.1109/JSTARS.2019.2923009.

[2] T. Liu, Z. Yang, A. Marino, G. Gao, and J. Yang, "PolSAR ship detection based on neighborhood polarimetric covariance matrix," *IEEE Trans. Geosci. Remote Sens.*, vol. 59, no. 6, pp. 4874–4887, Jun. 2021, doi: 10.1109/TGRS.2020.3022181.

[3] L. M. Novak, M. B. Sechtin, and M. J. Cardullo, "Studies of target detection algorithms that use polarimetric radar data," *IEEE Trans. Aerosp. Electron. Syst.*, vol. 25, no. 2, pp. 150–165, Mar. 1989. doi: 10.1109/7.18677.

[4] A. Marino, "A notch filter for ship detection with polarimetric SAR data," *IEEE J. Sel. Topics Appl. Earth Observ. Remote Sens.*, vol. 6, no. 3, pp. 1219–1232, Jun. 2013, doi: 10.1109/JSTARS.2013.2247741.

[5] T. Liu, Z. Yang, T. Zhang, Y. Du, and A. Marino, "A new form of the polarimetric notch filter," *IEEE Geosci. Remote Sens. Lett.*, vol. 19, 2022, Art no. 4001405, doi: 10.1109/LGRS.2020.3020052.

[6] F. Nunziata and M. Migliaccio, "On the COSMO-SkyMed pingpong mode to observe metallic targets at sea," *IEEE J. Ocean. Eng.*, vol. 38, no. 1, pp. 71–79, Jan. 2013, doi: 10.1109/JOE.2012.2210800.

[7] J. Chen, Y. Chen, and J. Yang, "Ship detection using polarization cross-entropy," *IEEE Geosci. Remote Sens. Lett.*, vol. 6, no. 4, pp. 723–727, Oct. 2009, doi: 10.1109/LGRS.2009.2024224.

[8] M. Migliaccio et al., "Marine added-value products using RADARSAT-2 fine quad-polarization," *Can. J. Remote Sens.*, vol. 37, no. 5, pp. 443–451, Mar. 2012.

[9] T. Zhang, Z. Yang, and H. Xiong, "PolSAR ship detection based on the polarimetric covariance difference matrix," *IEEE J. Sel. Topics Appl. Earth Observ. Remote Sens.*, vol. 10, no. 7, pp. 3348–3359, Jul. 2017, doi: 10.1109/JSTARS.2017.2671904.

[10] G. Gao and G. Shi, "CFAR ship detection in nonhomogeneous sea clutter using polarimetric SAR data based on the notch filter," *IEEE Trans. Geosci. Remote Sens.*, vol. 55, no. 8, pp. 4811–4824, Aug. 2017, doi: 10.1109/TGRS.2017.2701813.

[11] T. Liu, Z. Yang, A. Marino, G. Gao, and J. Yang, "Robust CFAR detector based on truncated statistics for polarimetric synthetic aperture radar," *IEEE Trans. Geosci. Remote Sens.*, vol. 58, no. 9, pp. 6731–6747, Sep. 2020, doi: 10.1109/TGRS.2020.2979252.

[12] G. Gao, K. Ouyang, Y. Luo, S. Liang, and S. Zhou, "Scheme of parameter estimation for generalized gamma distribution and its application to ship detection in SAR images," *IEEE Trans. Geosci. Remote Sens.*, vol. 55, no. 3, pp. 1812–1832, Mar. 2017, doi: 10.1109/TGRS.2016.2634862.

[13] G. Gao, S. Gao, J. He, and G. Li, "Adaptive ship detection in hybrid-polarimetric SAR images based on the power–entropy decomposition," *IEEE Trans. Geosci. Remote Sens.*, vol. 56, no. 9, pp. 5394–5407, Sep. 2018, doi: 10.1109/TGRS.2018.2815592.

[14] G. Gao, S. Gao, K. Ouyang, J. He, and G. Li, "Scheme for characterizing clutter statistics in SAR amplitude images by combining two parametric models," *IEEE Trans. Geosci. Remote Sens.*, vol. 56, no. 10, pp. 5636–5646, Oct. 2018, doi: 10.1109/TGRS.2018.2822759.

[15] G. Akbarizadeh, "A new statistical-based kurtosis wavelet energy feature for texture recognition of SAR images," *IEEE Trans. Geosci. Remote Sens.*, vol. 50, no. 11, pp. 4358–4368, Nov. 2012, doi: 10.1109/TGRS.2012.2194787.

[16] Z. Tirandaz and G. Akbarizadeh, "A two-phase algorithm based on kurtosis curvelet energy and unsupervised spectral regression for segmentation of SAR images," *IEEE J. Sel. Topics Appl. Earth Observ. Remote Sens.*, vol. 9, no. 3, pp. 1244–1264, Mar. 2016, doi: 10.1109/JSTARS.2015.2492552.

[17] F. Sharifzadeh, G. Akbarizadeh, and Y. Seifi Kavian, "Ship classification in SAR images using a new hybrid CNN–MLP classifier," *J. Indian Soc. Remote Sens.*, vol. 47, pp. 551–562, Apr. 2019, doi: 10.1007/s12524-018-0891-y.

[18] M. Iehara, K. Ouchi, I. Takami, K. Morimura, and S. Kumano, "Detection of ships using cross-correlation of split-look SAR images," in *Proc. IEEE Int. Geosci. Remote Sens. Symp.*, 2001, vol. 4, pp. 1807–1809, doi: 10.1109/IGARSS.2001.977078.

[19] A. Arnaud, "Ship detection by SAR interferometry," in *Proc. IEEE Int. Geosci. Remote Sens. Symp.*, 1999, vol. 5, pp. 2616–2618, doi: 10.1109/IGARSS.1999.771594.

[20] K. Ouchi, S. Tamaki, H. Yaguchi, and M. Iehara, "Ship detection based on coherence images derived from cross correlation of multilook SAR images," *IEEE Geosci. Remote Sens. Lett.*, vol. 1, no. 3, pp. 184–187, Jul. 2004, doi: 10.1109/LGRS.2004.827462.

[21] K. Ouchi and H. Wang, "Interlook cross-correlation function of speckle in SAR images of sea surface processed with partially overlapped subapertures," *IEEE Trans. Geosci. Remote Sens.*, vol. 43, no. 4, pp. 695–701, Apr. 2005, doi: 10.1109/TGRS.2004.842439.

[22] J.-C. Souyris, C. Henry, and F. Adragna, "On the use of complex SAR image spectral analysis for target detection: Assessment of polarimetry," *IEEE Trans. Geosci. Remote Sens.*, vol. 41, no. 12, pp. 2725–2734, Dec. 2003, doi: 10.1109/TGRS.2003.817809.
[23] C. H. Gierull, "Demystifying the capability of sublook correlation techniques for vessel detection in SAR imagery," *IEEE Trans. Geosci. Remote Sens.*, vol. 57, no. 4, pp. 2031–2042, Apr. 2019, doi: 10.1109/TGRS.2018.2870716.
[24] H. Greidanus, "Sub-aperture behavior of SAR signatures of ships," in *Proc. IEEE Int. Geosci. Remote Sens. Symp.*, Jul. 2006, pp. 3579–3582, doi: 10.1109/IGARSS.2006.917.
[25] R. Z. Schneider, K. P. Papathanassiou, I. Hajnsek, and A. Moreira, "Polarimetric and interferometric characterization of coherent scatterers in urban areas," *IEEE Trans. Geosci. Remote Sens.*, vol. 44, no. 4, pp. 971–984, Apr. 2006, doi: 10.1109/TGRS.2005.860950.
[26] A. Marino, M. J. Sanjuan-Ferrer, I. Hajnsek, and K. Ouchi, "Ship detection with spectral analysis of synthetic aperture radar: A comparison of new and well-known algorithms," *Remote Sens.*, vol. 7, no. 5, pp. 5416–5439, 2015, doi: 10.3390/rs70505416.
[27] C. Brekke, S. N. Anfinsen, and Y. Larsen, "Subband extraction strategies in ship detection with the subaperture cross-correlation magnitude," *IEEE Geosci. Remote Sens. Lett.*, vol. 10, no. 4, pp. 786–790, Jul. 2013, doi: 10.1109/LGRS.2012.2223656.
[28] M. J. Sanjuan-Ferrer, I. Hajnsek, K. P. Papathanassiou, and A. Moreira, "A new detection algorithm for coherent scatterers in SAR data," *IEEE Trans. Geosci. Remote Sens.*, vol. 53, no. 11, pp. 6293–6307, Nov. 2015, doi: 10.1109/TGRS.2015.2438173.
[29] A. Renga, M. D. Graziano, and A. Moccia, "Segmentation of marine SAR images by sublook analysis and application to sea traffic monitoring," *IEEE Trans. Geosci. Remote Sens.*, vol. 57, no. 3, pp. 1463–1477, Mar. 2019, doi: 10.1109/TGRS.2018.2866934.
[30] L. Ferro-Famil, A. Reigber, E. Pottier, and W. M. Boerner, "Scene characterization using sub-aperture polarimetric SAR data analysis," in *Proc. IEEE Int. Geosci. Remote Sens. Symp.*, 2002, vol. 1, pp. 417–419, doi: 10.1109/IGARSS.2002.1025058.
[31] L. Ferro-Famil, A. Reigber, E. Pottier, and W. M. Boerner, "Scene characterization using subaperture polarimetric SAR data," *IEEE Trans. Geosci. Remote Sens.*, vol. 41, no. 10, pp. 2264–2276, Oct. 2003, doi: 10.1109/TGRS.2003.817188.
[32] S. R. Cloude and K. P. Papathanassiou, "Polarimetric SAR interferometry," *IEEE Trans. Geosci. Remote Sens.*, vol. 36, no. 5, pp. 1551–1565, Sep. 1998, doi: 10.1109/36.718859.
[33] J. J. Wei, J. X. Zhang, G. M. Huang, and Z. Zhao, "A new ship detection method based on generalized multi-sublooks correlation using POLSAR data," *Acta Electronica Sinica*, vol. 44, no. 6, pp. 1516–1520, 2016, doi: 10.3969/j.issn.0372-2112.2016.06.037.
[34] T. Liu, J. Zhang, G. Gao, J. Yang, and A. Marino, "CFAR ship detection in polarimetric synthetic aperture radar images based on whitening filter," *IEEE Trans. Geosci. Remote Sens.*, vol. 58, no. 1, pp. 58–81, Jan. 2020, doi: 10.1109/TGRS.2019.2931353.
[35] R. Touzi, J. Hurley, and P. W. Vachon, "Optimization of the degree of polarization for enhanced ship detection using polarimetric RADARSAT-2," *IEEE Trans. Geosci. Remote Sens.*, vol. 53, no. 10, pp. 5403–5424, Oct. 2015, doi: 10.1109/TGRS.2015.2422134.
[36] R. Touzi and P. W. Vachon, "RCM polarimetric SAR for enhanced ship detection and classification," *Can. J. Remote Sens.*, vol. 41, no. 5, pp. 473–484, 2016.
[37] R. Touzi, J. Hurley, and P. W. Vachon, "Ship detection using polarimetric Radarsat-2," in *Proc. IEEE Asia-Pac. Conf. Synthetic Aperture Radar*, 2013, pp. 104–107.
[38] P. W. Vachon and J. Wolfe, "C-band cross-polarization wind speed retrieval," *IEEE Geosci. Remote Sens. Lett.*, vol. 8, no. 3, pp. 456–459, May 2011, doi: 10.1109/LGRS.2010.2085417.
[39] T. Liu, Y. Jiang, A. Marino, G. Gao, and J. Yang, "The polarimetric detection optimization filter and its statistical test for ship detection," *IEEE Trans. Geosci. Remote Sens.*, vol. 60, 2022, Art no. 5202218, doi: 10.1109/TGRS.2021.3055801.
[40] T. Liu, Z. Yang, A. Marino, G. Gao, and J. Yang, "Joint polarimetric subspace detector based on modified linear discriminant analysis," *IEEE Trans. Geosci. Remote Sens.*, vol. 60, 2022, Art no. 5223519, doi: 10.1109/TGRS.2022.3148979.
[41] M. Ester, "A density-based algorithm for discover erring clusters in large spatial databases with noise," *Proc. Knowl. Discov. Data Mining*, vol. 96, no. 34, pp. 226–231, 1996.

Ziyuan Yang received the B.S. degree in radar engineering in 2019 from the Naval University of Engineering, Wuhan, China, where he is currently working toward the Doctor's degree in information and communication engineering.

His research interests include radar polarization information process and electronic warfare system modeling and SAR ground moving target indication.

Lu Fang received the B.S. degree in electronic and information engineering and the M.S. degree in electronic and communication engineering from Yantai University, Yantai, China, in 2016 and 2019, respectively. She is currently working toward the Doctor's degree in information and communication engineering with the Naval University of Engineering, Wuhan, China.

Biao Shen received the B.S. degree in communication engineering in 2019 from the Naval University of Engineering, Wuhan, China, where he is currently working toward the Doctor's degree in information and communication engineering.

His research interests include polarization radar waveform design, radar polarization anti-jamming and radar polarization information process.

Tao Liu received the B.S. degree in communication engineering and the Ph.D. degree in information and communication engineering from the National University of Defense Technology, Changsha, China, in 2001 and 2007, respectively.

Since 2007, he has been with the School of Electronic Engineering, Naval University of Engineering, where he is currently a Professor. He has authored more than 50 journal papers and three books. His research interests include statistical theory of radar polarization, polarization information processing, synthetic aperture radar (SAR) automatic target recognition, statistical modeling of SAR image, SAR ship detection, InSAR (interferometric SAR), SAR ground moving target indication and artificial intelligence.